Journal of Materials Chemistry A

Accepted Manuscript

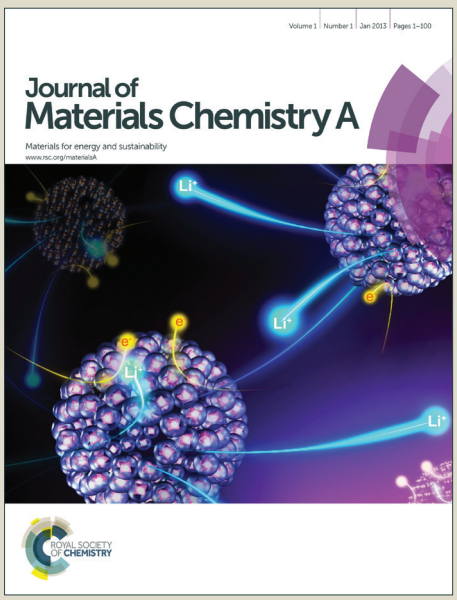

ROYAL SOCIETY OF CHEMISTRY

www.rsc.org/materialsA

Journal Name

ARTICLE

Fabrication of CeO_2/Fe_2O_3 composite nanospindles for enhanced visible light driven photocatalyst and supercapacitor electrode

Received 00th January 20xx,
Accepted 00th January 20xx

DOI: 10.1039/x0xx00000x

www.rsc.org/

N. Sabari Arul,[ab*] D. Mangalaraj,[b*] R. Ramachandran,[c] A. Nirmala Grace,[c] and Jeong In Han[a]

Hybrid CeO_2/Fe_2O_3 composite nanospindles (CNS) are synthesized by a simple and cost effective co-precipitation method. CeO_2/Fe_2O_3 CNS used as an efficient recyclable photocatalyst for degrading Eosin Yellow (EY) dye under visible light irradiation possess high degradation rate of 98% after 25 min. The estimated electrical energy efficiency of CeO_2/Fe_2O_3 CNS shows the consumption of less energy (6.588 $kWhm^{-3}$ $order^{-1}$) in degrading EY. Besides, the CeO_2/Fe_2O_3 CNS exhibits a specific capacitance of 142.6 F g^{-1} at a scan rate of 5 mV s^{-1}. Moreover, the composite displays excellent capacitance retention of 94.8% after 1000 cycles. This newly designed CeO_2/Fe_2O_3 CNS with enhanced visible light-driven photocatalytic activity and good supercapacitive cycling stability has great potential for use as wastewater treatment and energy storage applications.

1. Introduction

Semiconductor photocatalysis offers a green and energy-saving technology for the degradation of carcinogenic synthetic dyes in environmental and wastewater treatment.[1,2] Among eco-friendly photocatalytic materials, cerium oxide (CeO_2), a direct band gap semiconductor material has fascinated significant interest of researchers due to its wide band gap (~3.2) and considered as a potential material for photocatalyst,[3] fuel cells,[4] three-way catalyst,[5] sensors,[6] water treatment,[7] solar cells,[8] and electrochemical redox characteristics.[9] Despite, the photocatalytic property of the CeO_2 is predominantly restricted by the rapid recombination of the photo-induced electrons and hole.[10] To overcome this bottleneck, several approaches such as doping, noble metal loading and composites have been reported to reduce the charge recombination and enlarging the visible light exploitation of CeO_2 nanostructures.[11-13] Among them, CeO_2 based hybrid semiconductors have been designed to improve the absorption of photocatalysts in the visible light region.[14,15] Besides, electrochemical supercapacitor can store energy by near-surface ion adsorption with an additional contribution from fast reversible Faradic reaction, which offer them the desirable properties of high power density, rapid charge/discharge process and extensive lifespan.[16] CeO_2 nanorods and CeO_2/graphene based composites have been reported as the suitable candidate for high performance supercapacitor due to its better electrochemical redox characteristics, cost effective and eco- friendly material.[17-19]
Hematite (α-Fe_2O_3), as a direct bandgap (~2.1 eV) semiconductor material has been extensively used in water splitting and supercapacitor electrodes due to its high theoretical photocurrents under 1.5 A M illumination, sufficient stability and absorption capability in the visible light region.[20] Recently, fabrication of α-Fe_2O_3 heterojunctional composite with other semiconductor photocatalysts have been successfully hindered the recombination of the photogenerated electrons and holes resulting in the enhancement of photocatalytic degradation efficiencies.[16,21,22]
Even though, α-Fe_2O_3 is considered as one of the most promising pseudocapacitor electrode materials, the high-rate charge/discharge performance and cyclic stability are not fulfilled due to their poor electrical conductivity and metastability.[23,24] It is reasonable to speculate that combining Fe_2O_3 with CeO_2 may improve their catalytic activity, redox stability resulting in the enhanced performance in photocatalyst and electrochemical supercapacitor applications.[25] Based on the above consideration, we have attempted to exploit a new impressive visible light reactive hybrid CeO_2/Fe_2O_3 nanocomposite photocatalysts with a tailored bandgap for its potential application in photocatalyst and supercapacitors. However, to best of our knowledge the report on CeO_2/Fe_2O_3 hybrid composite nanospindles as potent visible light driven photocatalyst and high performance supercapacitor are limited up to date.

This study reports the data for CeO_2 nanoparticles (NPs), CeO_2/Fe_2O_3 composite nanospindles (CNS) and Fe_2O_3 nanorods (NRs) as potent visible light driven photocatalyst and high performance supercapacitor. Newly, Eosin yellow (EY) dye was chosen as an organic pollutant to evaluate the catalytic activity of CeO_2 NPs, CeO_2/Fe_2O_3 CNS, Fe_2O_3 NRs under visible light irradiation. The CeO_2/Fe_2O_3 CNS used as an excellent photocatalyst in degrading EY dye under visible light irradiation possessed a high degradation rate of 98% after 25 min. Besides, the CeO_2/Fe_2O_3 CNS exhibited a specific capacitance of 142.6 F g^{-1} at a scan rate of 5 mV s^{-1}. The fabricated CeO_2/Fe_2O_3 CNS showed an enhanced specific capacitance and photocatalytic degradation efficiency than pure CeO_2 NPs or Fe_2O_3 NRs.

[a] Department of Chemical and Biochemical Engineering, Dongguk University-Seoul, 100715, South Korea. Email: artsabari@gmail.com ; Tel: +82 2 2290 1646.
[b] Department of Nanoscience and Technology, Bharathiar University, Coimbatore, 641046, India. Email: dmraj800@yahoo.com ; Tel: +91 98947 62141.
[c] Centre for Nanotechnology Research, VIT University, Vellore, 632014, India.
†Electronic Supplementary Information (ESI) available. See
DOI: 10.1039/x0xx00000x

2. Experimental

2.1 Synthesis of CeO_2 NPs, CeO_2/Fe_2O_3 CNS and Fe_2O_3 NRs

CeO_2 NPs, CeO_2/Fe_2O_3 CNS and Fe_2O_3 NRs were prepared by a simple co-precipitation method.[26] Cerium (III) nitrate ($Ce(NO_3)_3.6H_2O$) and iron (II) nitrate ($Fe(NO_3)_2.6H_2O$), and ammonium hydroxide (NH_4OH) were purchased from Alfa Aesar. For the preparation of CeO_2/Fe_2O_3 CNS, required amount of cerium nitrate hexahydrate and iron nitrate hexahydrate were mixed together in stoichiometric proportions and precipitated by ammonia hydroxide solution (pH~11) under constant stirring at room temperature. The obtained colloidal solution was sealed in a beaker and aged for two days at ambient atmosphere. The resultant precipitates were separated by centrifuging at 6000 rpm and washed several times with ethanol and de-ionized water to remove the impurities. The precipitate was dried in vacuum oven at 90° C for overnight to obtain CeO_2/Fe_2O_3 CNS. A similar procedure was adopted to obtain pure CeO_2 NPs and Fe_2O_3 NRs.

2.2 Characterization techniques

The crystal structure of the CeO_2 NPs, CeO_2/Fe_2O_3 CNS and Fe_2O_3 NRs was determined by using Rigaku XRD/Max-2200 diffractometer with Cu-Kα radiation (λ = 0.15406 nm). The average crystal size of the obtained product was determined through X-ray diffraction (XRD) line broadening using the Scherrer equation. Transmission electron microscopy (TEM) was performed by using JEOL JEM-2100F system at an accelerating voltage of 200 kV. X-ray photoelectron microscopy (XPS) was performed using a Theta Probe AR-XPS System from Thermo Fisher Scientific with monochromated Al Kα (1486.6 eV) as an X-ray source operated at 15 kV. The light absorption properties of the catalysts were found using UV-vis spectroscopy. The UV-vis spectra were recorded on a Shimadzu UV-visible spectrophotometer- 3600.

2.3 Photocatalytic activity test

Photocatalytic activities of CeO_2 NPs, CeO_2/Fe_2O_3 CNS and Fe_2O_3 NRs photocatalysts were investigated by photodegradation of EY using a 150 W Xenon lamp under visible light illumination. 1 mg of catalysts was suspended in 30 ml containing 0.1 mM of the EY dye solution. Before illumination, the solution was ultrasonically agitated for 10 min in dark to achieve the equilibrium adsorption on the surface of the catalyst. Then, the solution was irradiated for various time intervals under visible light irradiation. The photodegradation studies were carried out by measuring the maximum absorption of EY at 481 nm using SHIMADZU 3600 UV-Vis-NIR spectrophotometer.

2.4 Electrochemical measurements

In this study, electrochemical measurements were carried out with an electrochemical analyzer (CHI 600C work station, version 5.01) using a three electrode system in 6 M KOH as the electrolyte solution under ambient conditions. CeO_2 NPs, CeO_2/Fe_2O_3 CNS and Fe_2O_3 NRs supported on the carbon paper (purchased from Cabot, USA), a platinum wire, and Ag/AgCl were utilized as the working electrode, counter and electrode, respectively. The cyclic voltammetry measurements were performed at various scan rates in the potential range from -0.3 to 0.3 V. The working electrode was prepared as follows: Initially, a required amount of pure or CeO_2/Fe_2O_3 CNS was dispersed in 5 wt% of nafion and then the mixture was coated on carbon paper with an area and mass of 0.5 cm x 0.5 cm and 2 mg cm^{-2}, respectively. The electrochemical impedance spectroscopy (EIS) spectrum was performed in the frequency range between 10 mHz and 1 MHz.

3. Results and discussion

The phase purity and crystal structures of the CeO_2 NPs, CeO_2/Fe_2O_3 CNS and Fe_2O_3 NRs were examined by XRD and the

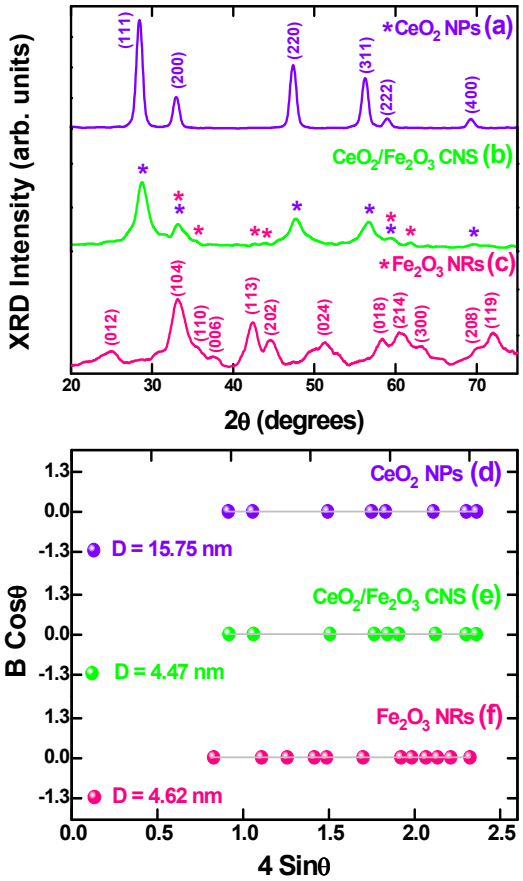

Fig. 1 XRD spectrum and Williamson-Hall plot of (a, d) CeO_2 NPs; (b, e) CeO_2/Fe_2O_3 CNS; (c, f) Fe_2O_3 NRs.

spectra are shown in Fig. 1(a-c). The diffraction peaks (violet and green line) along (111), (200), (220), (311), (222) and (400) planes confirms the cubic fluorite structure of CeO_2 which matches well with JCPDS PDF Card No. 34-0394. The XRD pattern of the CeO_2/Fe_2O_3 CNS (green line) reveals several new diffraction peaks emerging, which corresponds to the hexagonal α-Fe_2O_3 (JCPDS No 33-0664).[27] Furthermore, it rules out the possibility of any third phase formation confirming the formation of CeO_2/Fe_2O_3 composites which are consistent with the TEM images. All the diffraction peaks in the XRD pattern (pink line) of α-Fe_2O_3 can be indexed to the standard phase of the hexagonal α-Fe_2O_3.

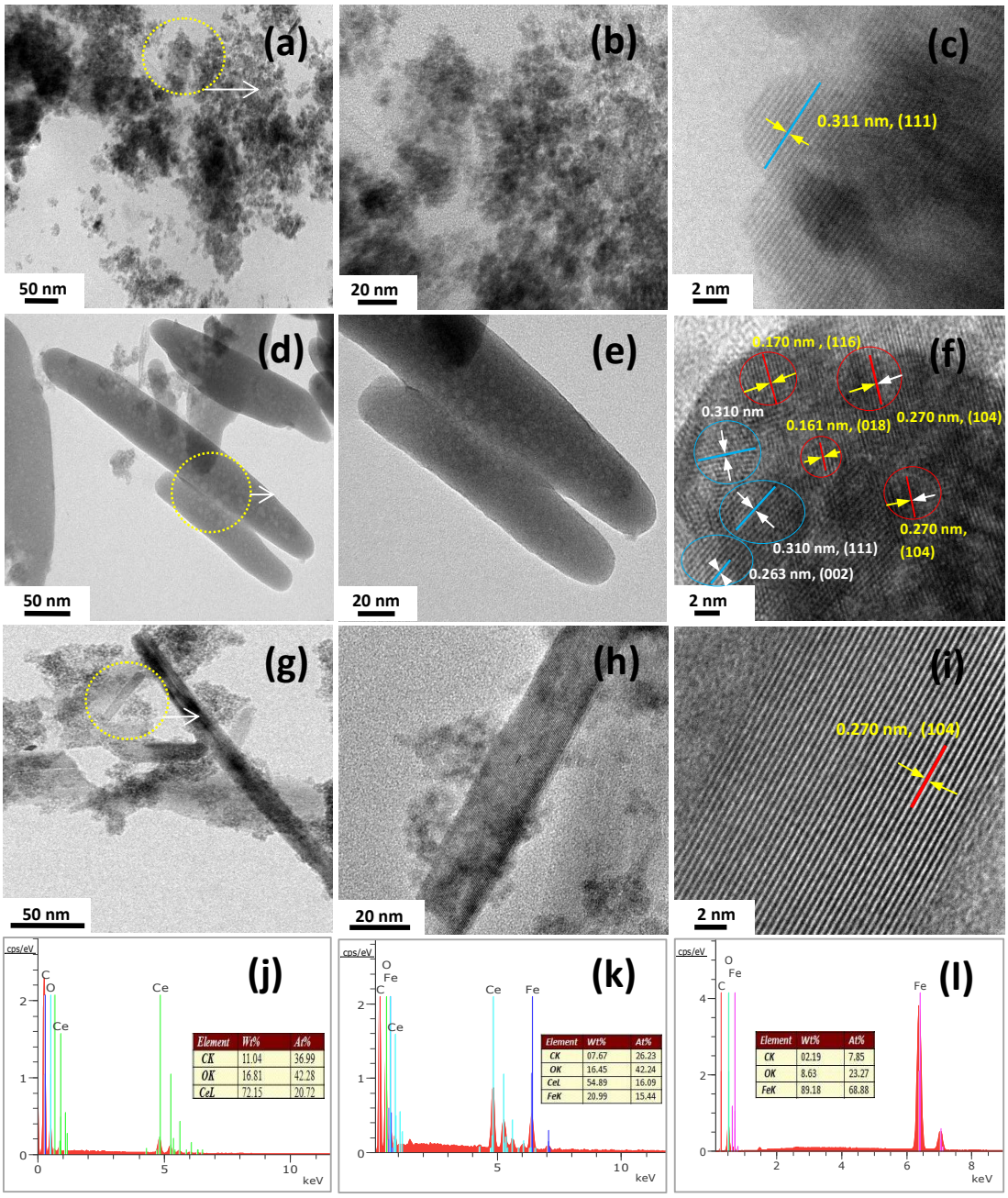

Fig. 2 TEM and HRTEM images of (a-c) CeO_2 NPs, (d-f) CeO_2/Fe_2O_3 CNS, (g-i) Fe_2O_3 NRs; (j, k, l) EDAX spectra of CeO_2 NPs, CeO_2/Fe_2O_3 CNS and Fe_2O_3 NRs.

The crystallite size of CeO_2 NPs, CeO_2/Fe_2O_3 CNS and Fe_2O_3 NRs are estimated by using Williamson-Hall (W-H) plots. The correction for peak broadening (B) of each plane is given as;

$$B^2 = (\beta^2_{experimental} - \beta^2_{instrumental}) \quad (1)$$

where the width ($\beta^2_{experimental}$) of each peak is measured as the integral breadth and the instrumental broadening ($\beta^2_{instrumental}$) is determined from polycrystalline silicon standard.

The Williamson-Hall equation is given as,[28]

$$B \cos\theta = K\lambda / D + 2\varepsilon \sin\theta \quad (2)$$

where D is the coherent scattering length (crystallite size); K is the shape factor (0.9); λ is the wavelength of X-Ray source (1.54Å), B is the integral width of the sample (in rad) estimated from eq. (1), θ is the angle of reflection (in deg) and ε is the inhomogeneous internal strain (in %). Fig. 1(d-f) shows the W-H plot for the synthesized CeO_2 NPs, CeO_2/Fe_2O_3 CNS and Fe_2O_3 NRs. Thus, the crystallite size calculated from W-H plot is found to be 15.75, 4.47 and 4.62 nm, respectively. It can be seen that, the full-width-at-half-maximum (FWHM) of the diffraction peaks of CeO_2/Fe_2O_3 CNS was found to be substantially larger than those of pure CeO_2 NPs implying a decreased crystallite size.

Fig. 2(a) and 2(b) shows TEM images of pure CeO_2 NPs with an average diameter of 10 nm. Fig. 2(c) displays a typical high resolution TEM (HRTEM) image of CeO_2 NPs with an

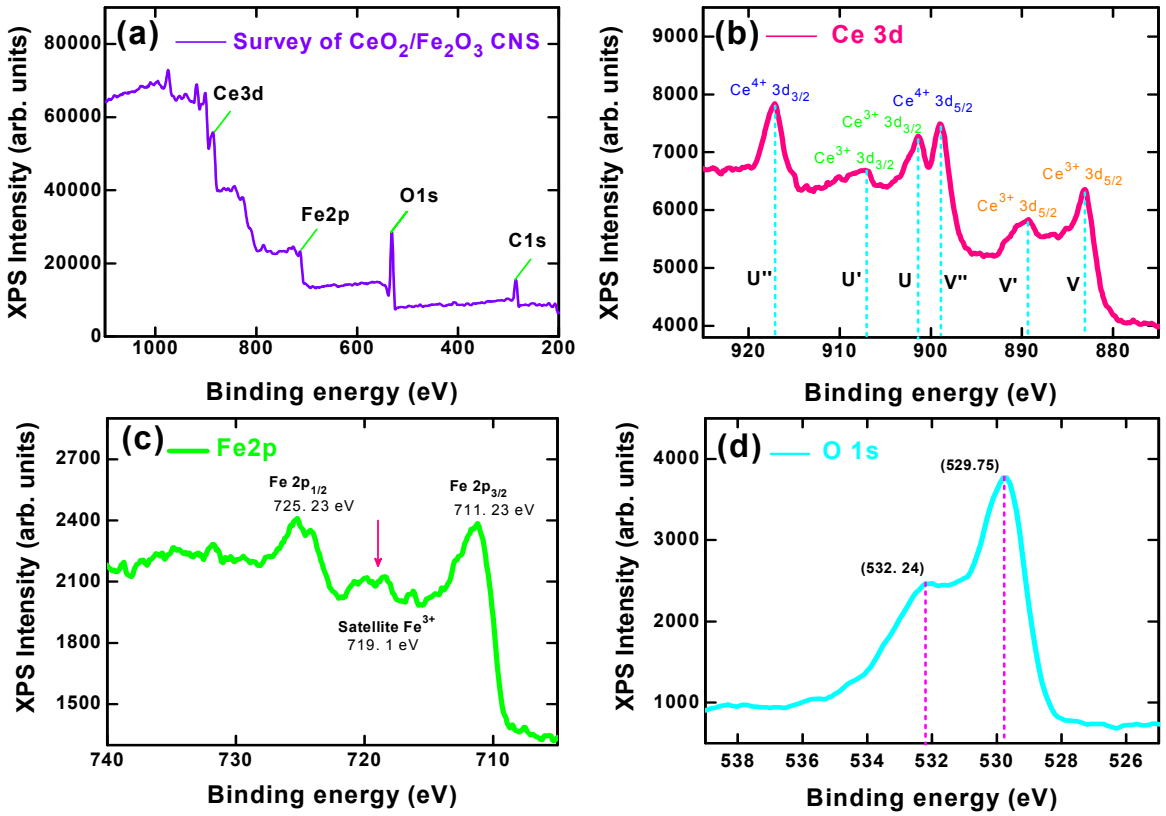

Fig. 3 (a) Representative XPS survey spectrum of CeO_2/Fe_2O_3 CNS; high resolution XPS spectra of (b) Ce 3d; (c) Fe 2p; (d) O 1s.

interplanar spacing distance of 0.311 nm correspond to the (111) plane of cubic CeO_2 (JCPDS 34-0394). TEM images of the CeO_2/Fe_2O_3 CNS are displayed in Fig. 2(d) and 2(e), it can be seen that the CeO_2/Fe_2O_3 CNS have the spindle like nanostructures. The size of nanospindles is about 40-60 nm in diameter and 200-300 nm in length. Fig. 2(f) illustrates the HRTEM image of CeO_2/Fe_2O_3 CNS, it is observed that the CeO_2/Fe_2O_3 CNS is made up of CeO_2 nanoparticles with an interplanar spacing distance of 0.310 and 0.263 nm corresponds to (111) and (200) plane of cubic CeO_2 and α-Fe_2O_3 nanoparticles with lattice spacing of 0.270, 0.170 and 0.161 nm attributes to the (104), (116) and (018) planes of α-Fe_2O_3 (JCPDS No 33-0664).[29,30] TEM images of the Fe_2O_3 NRs are shown in Fig. 2(g) and 2(h). It can be observed that the size of the nanorods is about 10-20 nm in diameter and 50-300 nm in length. Besides, few nanoparticles are also observed on the surface of the Fe_2O_3 NRs with size less than 10 nm. Fig. 2(i) illustrate the HRTEM image of Fe_2O_3 NRs with lattice fringe of 0.270 nm correspond to (104) lattice spacing of α-Fe_2O_3.

Scheme 1 shows the possible growth mechanism of the synthesized nanostructures. Firstly, possible growth mechanism of α-Fe_2O_3 NRs is as follows; (a) tiny primary nanocrystals were produced due to the presence of excess OH^- and (b) agglomeration and coarsening of α-Fe_2O_3 primary nanocrystals tends to grow into rod-like nanostructures, possibly motivated by oriented attachment.[31,32] Secondly, TEM images of CeO_2/Fe_2O_3 composites (Fig. 2(d),(e)) displays the formation of spindles like nanostructures where the nuclei grow into primary nanocrystals leads to the agglomeration and coarsening of CeO_2/Fe_2O_3 primary nanocrystals tends to grow into rod-like nanostructures, which might be attributed to an oriented attachment.[33] Furthermore, the nanospindle architecture is obtained from the abundant nanorod-like building blocks and their corresponding geometrical illustration is denoted in Scheme 1, Left corner.

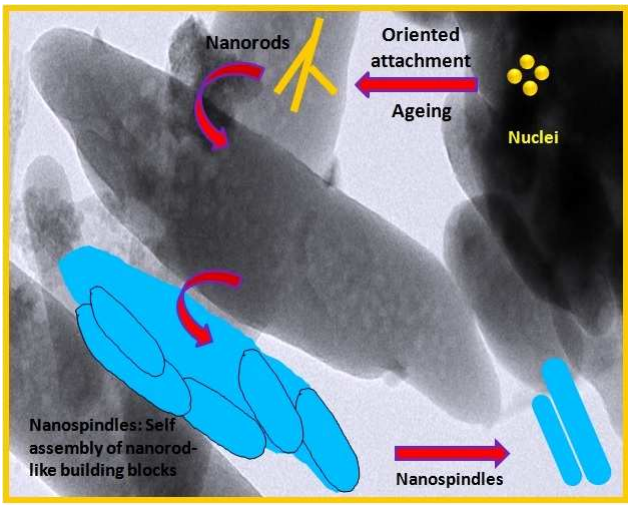

Scheme 1 shows the possible growth mechanism of the synthesized nanostructures.

Thus, the observation suggests that the formation of spindle-like nanostructures appears to be driven by minimization of the overall surface energies through orientation attachment determined by the self-assembly of the nanorods.[34,35]

The elemental compositions of CeO_2 NPs, CeO_2/Fe_2O_3 CNS and Fe_2O_3 NRs were also determined by EDAX profile, as shown in Fig. 2(j-l). The inset of Fig. 2(j) displays the elemental composition of the CeO_2 NPs and is found to be 72.15 wt% of Ce, 16.81 wt% of O and 11.04 wt% of C (Carbon). inset of Fig. 2(k) show the elemental composition of the CeO_2/Fe_2O_3 CNS is found to be 20.99 wt% of Fe, 54.89 wt% of Ce, 16.45 wt% of O and 7.67 wt% of C (Carbon). Thus, the EDAX spectra of pure CeO_2 and CeO_2/Fe_2O_3 CNS are consistent with XRD and TEM results. The inset of Fig. 2(l) shows the elemental composition of the Fe_2O_3 NRs and is found to be 89.18 wt% of Fe, 8.63 wt% of O and 2.19 wt% of C (Carbon).

The XPS analysis was utilized to investigate the chemical states of Ce, Fe and O in CeO_2/Fe_2O_3 CNS. The wide survey spectrum in Fig. 3(a) illustrates the binding energy peaks at 287.2, 530.6, 710.5 and 885.8 eV, which are attributed to C 1s, O 1s, Fe 2p and Ce 3d, respectively. Fig. 3(b-d) shows the high–resolution XPS spectra of Ce 3d, O 1s and Fe 2p peaks. The Ce 3d core level spectrum is shown in Fig. 3(b), exhibits both Ce^{3+} and Ce^{4+} oxidation state due to the splitting of spin doublets ($3d_{3/2}$ and $3d_{5/2}$ orbit).[36] The main peaks of $Ce^{4+}3d_{3/2}$ and $Ce^{4+}3d_{5/2}$ lie at the binding energies of 916.14 and 898.43 eV, respectively. The $Ce^{3+}3d_{3/2}$ appears at 886.85 eV with a shakeup satellite peak at about 907.1 eV and $Ce^{3+}3d_{5/2}$ allocated at 903.8 eV with two satellite peaks at 883.11 and 889.37 eV, respectively. The Ce 3d spectrum is consistent with earlier reports.[37] The high resolution Fe 2p peak of the CeO_2/Fe_2O_3 CNS is depicted in Fig. 3(c). The binding energies of 711.23 and 725.23 eV are indicative of Fe $2p_{3/2}$ and Fe $2p_{1/2}$, which is in good agreement with the earlier reports.[35] The existence of shakeup satellite features for Fe^{3+} rules out the possibility of the standard Fe_2O_3 phase presence in the CeO_2/Fe_2O_3 CNS.[38,39] The broad O 1s peak at 529.75 and 532.24 eV is assigned to surface adsorbed oxygen, oxygen from CeO_2, oxygen from Ce_2O_3, $Ce(OH)_3$ and $Ce(OH)_4$, respectively.[40,41] The XPS data indicate that the Fe_2O_3 nanoparticles are successfully incorporated into the CeO_2 nanoparticles, which is consistent with XRD and EDAX results. The UV-visible absorbance spectroscopy of CeO_2 NPs, CeO_2/Fe_2O_3 CNS and Fe_2O_3 NRs was shown in Fig. 4. The band gap E_g was calculated by using the equation, $E_g = 1240/\lambda_{(nm)}$, where E_g is the band gap (eV) and $\lambda_{(nm)}$ is the wavelength of the absorption edge in the spectrum.[42] It can be observed that the CeO_2/Fe_2O_3 CNS can absorb UV and visible light with wavelength less than 600 nm, corresponding to the band gap energy of 2.11 eV and while the absorption band edge of pure CeO_2 NPs and Fe_2O_3 NRs were located at 440 nm and 565 nm, corresponds to a band gap energy of 2.8 eV and 2.21 eV, respectively. The absorption of CeO_2/Fe_2O_3 CNS shows broad visible-light absorption, which might be favorable for the photodegradation efficiency.[43]

The photodegradation experiments were conducted to reveal the photocatalytic activity of the as-prepared CeO_2 NPs, CeO_2/Fe_2O_3 CNS and Fe_2O_3 NRs (catalysts) for the degradation of EY dye. Fig. 5(a-c) shows the absorption curves during the photocatalytic activity of EY with catalysts under visible light irradiation.

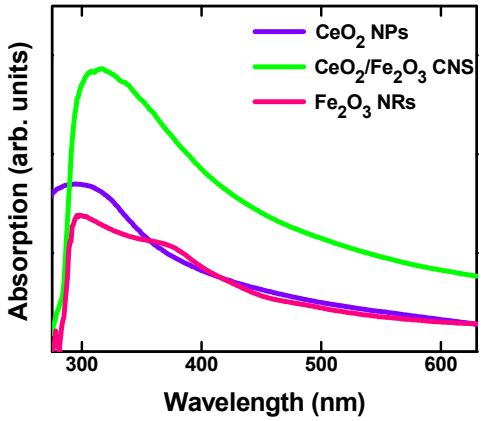

Fig. 4 UV-visible absorption spectroscopy of CeO_2 NPs, CeO_2/Fe_2O_3 CNS and Fe_2O_3 NRs.

The absorption peak intensity gradually decreases with increasing exposure time from 0 to 25 min. Fig. 5(d) displays the photodegradation efficiencies of blank EY and EY with catalysts under visible light irradiation. The results show that the decrease in the EY dye concentration without a photocatalyst (blank) is exceptionally low and only 0.32% of EY is degraded in the dark for 25 min. However, in the presence of photocatalyst, the degradation of EY increases gradually with increasing irradiation time. Furthermore, it can be seen that 98% of the EY dye are degraded after 25 min irradiation for the hybrid CeO_2/Fe_2O_3 CNS. Nevertheless, the degradation efficiency of CeO_2 NPs and Fe_2O_3 NRs catalyst are only 69 and 53%, respectively. Fig. 5(e) shows the experimental and the linear plot of $\ln(A_o/A_t)$ as a function of the irradiation time (t) for EY with the catalysts. The degradation in the EY dye molecule catalyzed by catalysts fits the pseudo-first-order equation (4);[44]

$$\ln (A_o/A_t) = k_{app}\, t \qquad (4)$$

where A_o is the initial concentration of EY, A_t is the final concentration of EY, and k_{app} is the apparent rate constant of the pseudo-first-order reaction. The estimated apparent rate constant of CeO_2 NPs, CeO_2/Fe_2O_3 CNS and Fe_2O_3 NRs from the slope of the plot $\ln(A_o/A_t)$ versus t are found to be 0.0461, 0.1167 and 0.0289 min^{-1}. The CeO_2/Fe_2O_3 CNS displays an excellent photocatalytic activity with a degradation rate of 98% after 25 min for EY dye under visible light illumination. Yet, the long-term stability of the photocatalytic systems is most essential for the real world consideration.

Figure 5f shows the recyclable photodegradation experiments of EY in presence of CeO_2/Fe_2O_3 CNS for 1-4 cycles under visible light irradiation. From the results it is clear that the CeO_2/Fe_2O_3 CNS exhibits an excellent stability with less than 10% decrease from its initial activity to final photocatalytic degradation process. The half-life time ($t_{1/2}$) is the amount of time required for 50% of dye concentration to degrade and it is given by Eq. (5); [45]

$$t_{1/2} = 1n\ 2/k_{app} \qquad (5)$$

where k_{app} is the apparent rate constant of the pseudo-first-order reaction. The estimated $t_{1/2}$ values are found to be 6.529, 2.579 and 10.415 min, respectively (Table 1).

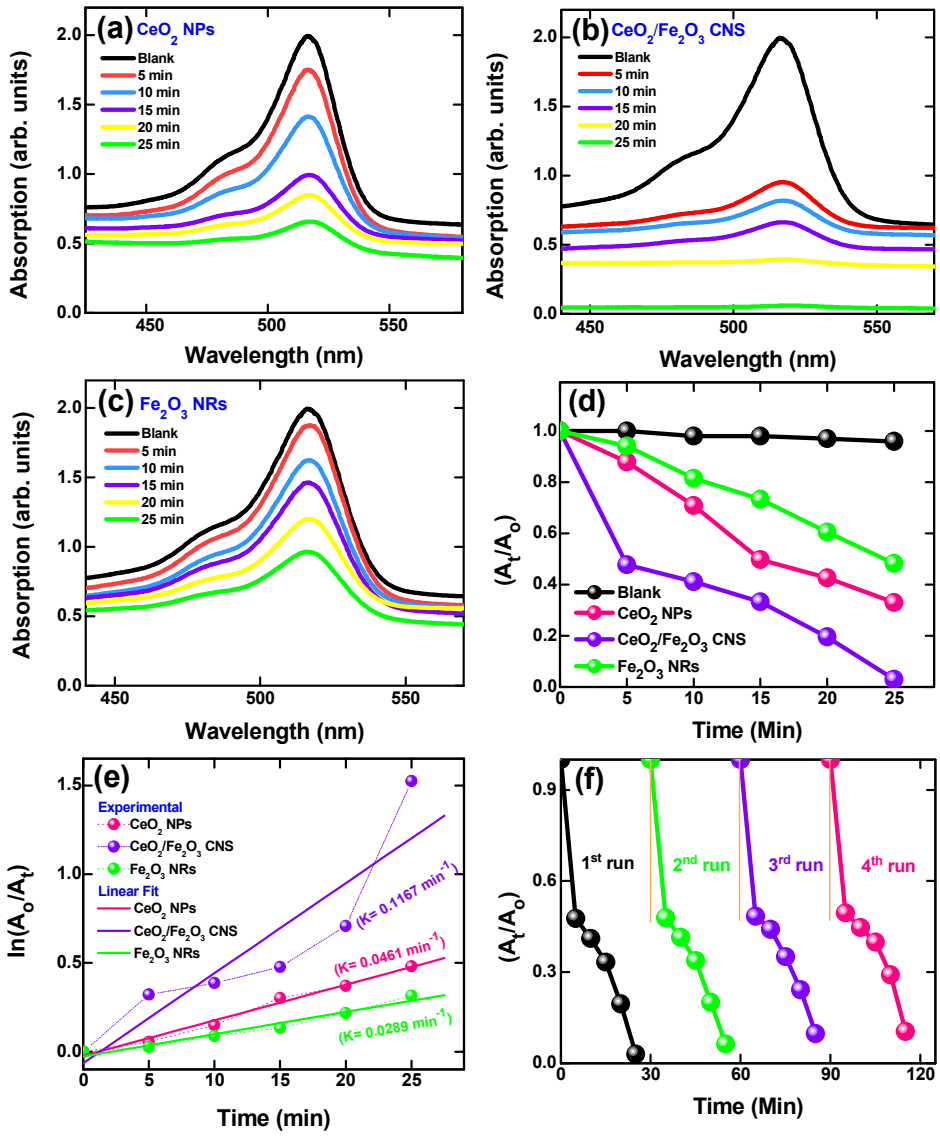

Fig. 5 Ultraviolet-visible absorbance spectra of EY dye solutions with (a) CeO_2 NPs, (b) CeO_2/Fe_2O_3 CNS, (c) Fe_2O_3 NRs for various photodegradation time intervals; (d) Degradation efficiency of the blank, EY with CeO_2 NPs, CeO_2/Fe_2O_3 CNS and Fe_2O_3 NRs catalyst versus irradiation time; (e) Experimental and linear plot of ln (A_o/A_t) as a function of the irradiation time for CeO_2 NPs, CeO_2/Fe_2O_3 CNS and Fe_2O_3 NRs catalyst and (f) recyclable test of CeO_2/Fe_2O_3 CNS CNS in degrading EY dye under visible light irradiation.

Table 1 Calculated photodegradation parameters of the obtained catalysts (error±0.003)

Materials	K (min^{-1})	R^2	$T_{1/2}$ (min)	E_{EO} ($kWhm^{-3}$ $order^{-1}$)
CeO_2 NPs	0.046	0.982	6.529	20.85
CeO_2/Fe_2O_3 CNS	0.116	0.784	2.579	6.588
Fe_2O_3 NRs	0.028	0.956	10.415	31.78

The electrical energy per order (E_{EO}) is considered to estimate the electrical energy required to remove unit mass of pollutant.[46] The E_{EO} is defined as the number of kilowatt hours of electrical energy required to degrade the concentration of dye by one order of magnitude (90%) in $1m^3$ of the contaminated water, and the equation is expressed as follows (6);

$$E_{EO} = (P \times t \times 1000)/ [V \times 60 \times \log (A_o/A_t)] \quad (6)$$

where, P is the rated power (kW) of the advanced oxidation process system, t is the irradiation time (min), V is the volume (L) of the water, ln (A_o/A_t) = k_{app} t, A_0 and A_t are the initial and final pollutant concentrations. The evaluated E_{EO} value of CeO_2 NPs, CeO_2/Fe_2O_3 CNS and Fe_2O_3 NRs catalysts are found to be 20.85, 6.588 and 31.78 $kWhm^{-3}$ $order^{-1}$, respectively. The low E_{EO} value of CeO_2/Fe_2O_3 CNS catalysts confirms that less energy is enough to attain excellent photo

degradation efficiency in CeO_2/Fe_2O_3 CNS. Our results indicate that, the CeO_2/Fe_2O_3 CNS has great potential for use as a visible light driven photocatalyst.

Fig. 6 shows the proposed photocatalytic degradation mechanism of CeO_2/Fe_2O_3 CNS. The band edge position of the conduction band (CB) and valence band (VB) of a semiconductor can be determined using the equation (7); [47]

$$E_{VB} = \chi - E_e + 0.5\ E_g \quad (7)$$

where χ is the absolute electronegativity of the semiconductor (χ_{CeO2} = 5.57 eV and χ_{Fe2O3} = 5.87 eV), E_e is Energy of free electrons on the hydrogen scale (ca. 4.5 eV), E_{VB} is the VB edge potential and E_g is the energy band gap of the semiconductor CeO_2 (2.8 eV) and Fe_2O_3 (2.21 eV). The CB position can be deduced by $E_{CB} = E_{VB} - E_g$. The estimated CB and VB of CeO_2 are 2.775 and -0.035 eV and it is beneficial than those of the Fe_2O_3 are 2.475 and 0.265 eV, respectively.

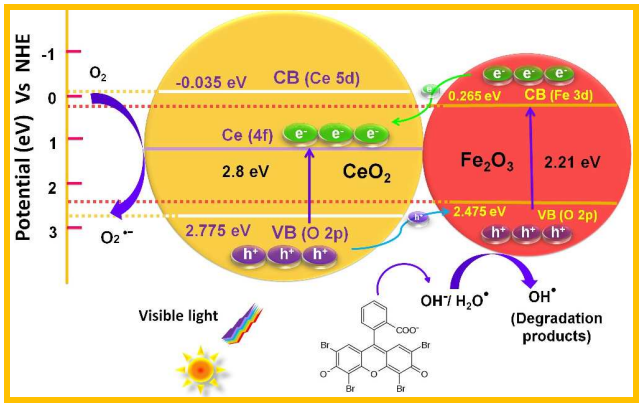

Fig. 6 Proposed photodegradation mechanism of CeO_2/Fe_2O_3 CNS in degrading EY dye under visible light irradiation.

During photodegradation process, the electrons from the valance band of CeO_2 NPs (2.8 eV) can migrate easily to the conduction band by absorbing visible light.[48] Those electrons accumulated on the surface of the CeO_2 NPs are then scavenged by O_2 molecules absorbed on the surface of the product and yield superoxide anion ($O_2^{\bullet-}$), which are responsible for the photodegradation of EY dye. Similarly, in case of CeO_2/Fe_2O_3 CNS (Fig. 6), the photogenerated holes from CeO_2 migrate to the VB of Fe_2O_3, while the photogenerated electrons in Fe_2O_3 transfer to the CB of CeO_2. Besides, the holes in the VB of Fe_2O_3 readily oxidize OH^- species or $H_2O^{\bullet}$ producing reactive hydroxyl ($^{\bullet}OH$) radicals, which are further involved in the photodegradation of EY. This reaction can be given by (8);

$$h^+_{VB} + OH^- \rightarrow OH^{\bullet} \quad (8)$$

In the meantime, the gathered electrons in the CB of CeO_2 can be migrated to O_2 molecules absorbed on the surface of the product and yield superoxide anion ($O_2^{\bullet-}$), the equation is given by (9);

$$e^-_{CB} + O_2 \rightarrow O_2^{\bullet-} \quad (9)$$

Lastly, the formed $^{\bullet}OH$ and $O_2^{\bullet-}$ act as a effective oxidizing agent in degrading EY dye and represented in the equation as follows (10);

$$(OH^{\bullet}, O_2^{\bullet-}) + \text{EY dye} \rightarrow \text{Degradation of EY dye} \quad (10)$$

Our results showed that the formation of CeO_2/Fe_2O_3 CNS hinder the recombination of photo-induced charge carries and promote the generation of more $OH^{\bullet}$ radicals resulting in the enhancement of photodegradation efficiency of CeO_2/Fe_2O_3 CNS.

Finally, to demonstrate the possible application of CeO_2/Fe_2O_3 CNS as supercapacitor electrode, the electrochemical performance and charge storage mechanism of CeO_2 NPs, CeO_2/Fe_2O_3 CNS, Fe_2O_3 NRs and bare carbon are investigated in three electrode systems with 6 M KOH electrolyte. Fig. 7(a-c) shows the cyclic voltammetry (CV) curves of electrodes at various scan rates (5-100 mV s^{-1}) in the potential range of -0.3 to 0.3 V. The quasi rectangular shapes of CV curves are evidently observed, indicating the existence of dual behavior of electric double layer and pseudocapacitance nature of the electrodes.[49] The non-faradic reaction of CeO_2 and Fe_2O_3 may be due to the formation of double layer at the electrode/electrolyte interfaces during insertion/deinsertion of positive ions (K^+) and the reaction is described by equation (11 and 12) as follows;

$$(CeO_2)surface + K^+ + e^+ \leftrightarrow (CeO_2 - K^+)surface \quad (11)$$

$$(Fe_2O_3)surface + K^+ + e^+ \leftrightarrow (Fe_2O_3 - K^+)surface \quad (12)$$

In addition, the faradic reaction process is also observed in the electrodes, which causes a slight deviation of rectangular shape in the CV curves for all scan rates due to the reversible reactions of Fe^{2+}/Fe^{3+} and Ce^+/Ce^{2+} associated with OH^- anions.[50] The equation for the possible reversible process can be explained as follows (13 and 14);

$$CeO_2 + OH^- \leftrightarrow CeO_2OH + e^- \quad (13)$$

$$Fe_2O_3 + OH^- \leftrightarrow Fe_2O_3OH + e^- \quad (14)$$

The area of the CV curve reflects the capacitance and the real active surface area of the materials.[51] Fig. 7(d) displays CV curve of CeO_2 NPs, CeO_2/Fe_2O_3 CNS & Fe_2O_3 NRs at a scan rate of 50 mV s^{-1}. A larger area and high current response are observed for CeO_2/Fe_2O_3 CNS electrode than those of bare carbon, CeO_2 NPs and Fe_2O_3 NRs electrodes. Besides, the area of the CV curve for bare carbon electrode is very low and hence its capacitance contribution will be negligible. As well, the specific capacitance (C) and energy density (E) of electrode materials are calculated from the CV curves according to the following formula (15 and 16);[52]

$$C = \frac{(I_+ - I_-)}{mv} \quad (15)$$

$$E = \frac{1}{2}CV^2 \quad (16)$$

where, C is specific capacitance (F g^{-1}), E is energy density (Wh kg^{-1}), I_+ is the maximum current in the positive scan (A), I_- is the maximum current in the negative scan (A), 'm' the mass of the active material (g), 'u' is the scan rate (V s^{-1}) and V is initial voltage (V). The CeO_2/Fe_2O_3 CNS shows a high specific capacitance of 142.6 F g^{-1} at 5 mV s^{-1} while for the CeO_2 NPs and Fe_2O_3 NRs exhibited minimum specific capacitance of 28.1 and 82.2 F g^{-1}, respectively.

The specific capacitance of electrodes decreases with increase in scan rate and it is evident from Fig. 8. The positive ions (K^+) can easily diffuse into the available spaces of electrodes, lead to sufficient insertion reaction at lower scan rates. On the other hand, at higher scan rates, positive ions can approach only the outer surface of electrodes resulting in a slight deviation of CV curve with less specific capacitance.[53] High energy density of 6.41 Wh kg^{-1} is observed for CeO_2/Fe_2O_3 CNS, while 1.26 and 3.69 Wh kg^{-1} attributes to the low energy density of CeO_2 NPs and Fe_2O_3 NRs electrodes. The enhancement of electrochemical performance can be attributed to the synergistic effect of CeO_2/Fe_2O_3 composite, which accelerates the ion/electron transfer.[16]

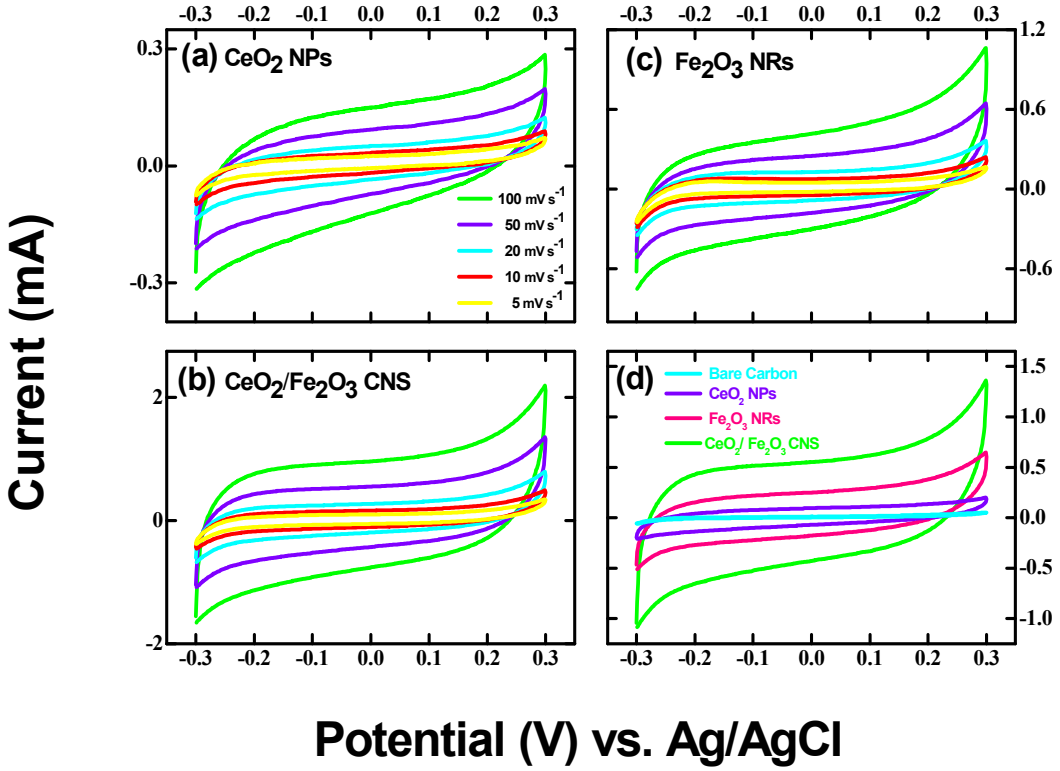

Fig. 7 Cyclic voltammetry curves of (a) CeO_2 NPs, (b) CeO_2/Fe_2O_3 CNS, (c) Fe_2O_3 NRs with different scan rates; (d) Typical CV curves of CeO_2 NPs, CeO_2/Fe_2O_3 CNS, Fe_2O_3 NRs and bare carbon electrodes at scan rate of 50 mV s^{-1}.

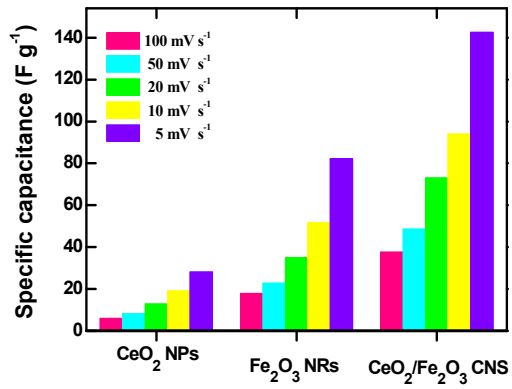

Fig. 8 Comparison of specific capacitance at various scan rates of CeO_2 NPs, CeO_2/Fe_2O_3 CNS and Fe_2O_3 NRs electrodes.

The galvanostatic charge/discharge analysis is a reliable method for the evaluation of electrochemical performance of electrodes under constant current conditions. Fig. 9(a) shows the typical charge/discharge curves of bare carbon, CeO_2 NPs, CeO_2/Fe_2O_3 CNS and Fe_2O_3 NRs electrodes at a current density of 0.5 A g^{-1}. The charge/discharge curves of CeO_2/Fe_2O_3 CNS at various current densities are given in Fig. 9(b). A slight deviation in symmetric charge-discharge curves is observed from Fig. 9(a) and 9(b), signifying the dual behavior of electric double layer and pseudocapacitance nature of the electrodes.[49,54] The charge/discharge curve of CeO_2/Fe_2O_3 CNS show low IR drop than those of CeO_2 NPs and Fe_2O_3 NRs electrodes, suggesting the large pseudocapacitance nature and less energy dissipated during charge-discharge process.[55] The cycling stability of CeO_2 NPs, CeO_2/Fe_2O_3 CNS and Fe_2O_3 NRs at 50 mV s^{-1} for 1000 cycles is presented in Fig. 9c. It is observed that, CeO_2/Fe_2O_3 CNS electrode possesses large capacitance retention of 94.8 % than those of CeO_2 NPs and Fe_2O_3 NRs, indicating the high stability of the CeO_2/Fe_2O_3 CNS electrode. To further explore the electrochemical behaviors of CeO_2 NPs, CeO_2/Fe_2O_3 CNS and Fe_2O_3 NRs electrodes, electrochemical impedance spectroscopy (EIS) is measured in the frequency range between 10 mHz and 1 MHz. Fig. 9(d) shows the EIS spectra of CeO_2 NPs, CeO_2/Fe_2O_3 CNS and Fe_2O_3 NRs electrodes with a depressed semicircle and a single vertical line observed in the high frequency region. The depressed arc at high frequency attributes to the charge transfer resistance (R_{CT}) occurring at the electrode/electrolyte interfaces.[56,57] The EIS spectra are fitted using the equivalent circuit represented in the inset of Fig. 9(d). The calculated values of R_s are found to be 7.24, 2.83 and 2.74 Ω for CeO_2 NPs, CeO_2/Fe_2O_3 CNS and Fe_2O_3 NRs electrodes, respectively. In addition, the estimated R_{CT} values are 1.287, 0.09 and 0.15 Ω. The lower value of R_s and R_{CT} obtained for the CeO_2/Fe_2O_3 CNS electrode suggesting the fast electron transfer process and improved ionic conductivity at the electrode/electrolyte interface in the CeO_2/Fe_2O_3 CNS electrode.

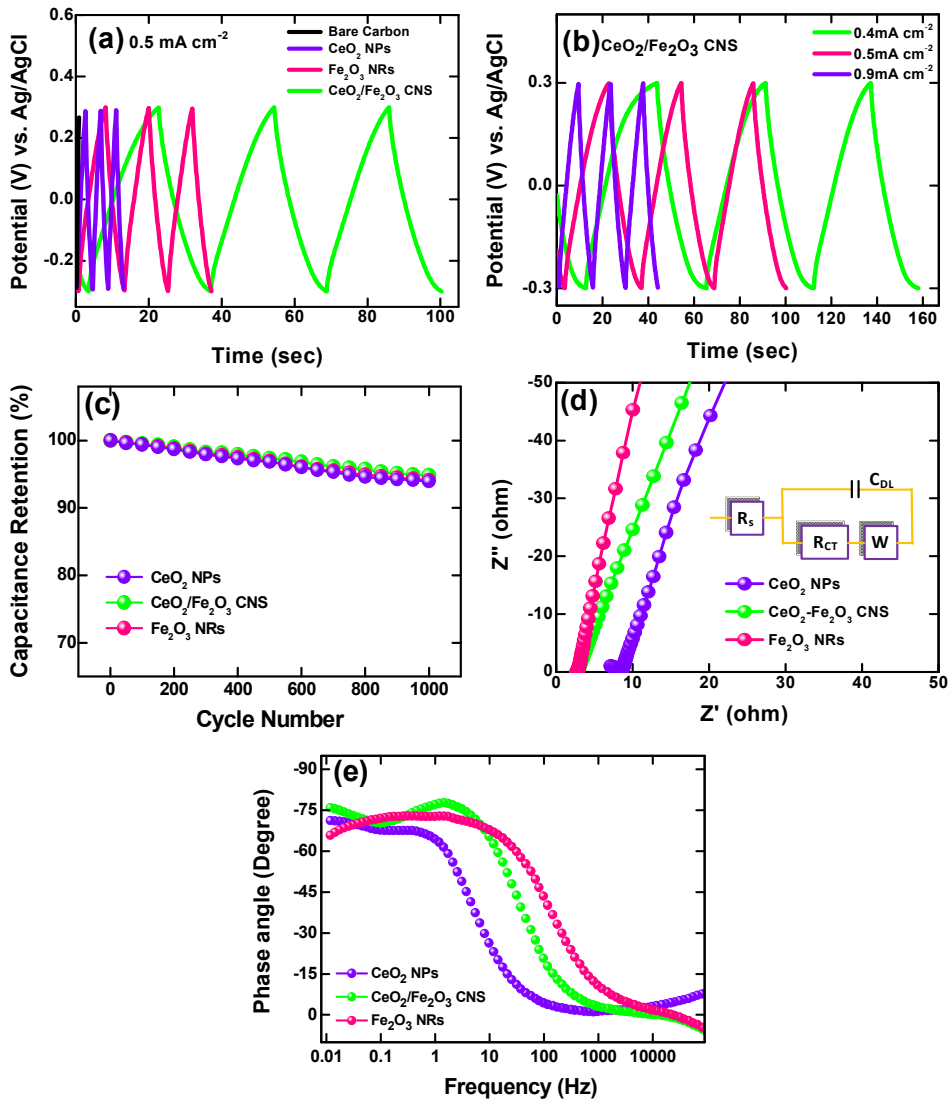

Fig. 9 (a) Galvanostatic charge/discharge curves of CeO_2 NPs, CeO_2/Fe_2O_3 CNS, Fe_2O_3 NRs and bare carbon electrodes at 0.5 A g^{-1}; (b) Galvanostatic charge/discharge curves CeO_2/Fe_2O_3 CNS at different current densities; (c) Capacitance retention of CeO_2 NPs, CeO_2/Fe_2O_3 CNS and Fe_2O_3 NRs electrodes electrodes as function of cycle number measured at a scan rate of 50 mV s^{-1}; (d) Nyquist Plots, (e) Variation of phase angle with respect to frequency of CeO_2 NPs, CeO_2/Fe_2O_3 CNS and Fe_2O_3 NRs electrodes.

Fig. 9(e) shows the variation of the phase angle as a function of frequency and lies in the range of 66-75°, which attributes to the partial redox and capacitive nature of the CeO_2 NPs, CeO_2/Fe_2O_3 CNS and Fe_2O_3 NRs materials.[58] Our electrochemical results showed that, the CeO_2/Fe_2O_3 CNS has great potential for use as a supercapacitor electrode material.

4. Conclusions

CeO_2 NPs, CeO_2/Fe_2O_3 CNS and Fe_2O_3 NRs were synthesized by solution processed co-precipitation method and investigated its photocatalytic and supercapacitive properties. Among all, the CeO_2/Fe_2O_3 CNS showed an enhanced degradation efficiency of 98% after 25 min in degrading EY under visible light irradiation. In addition, the calculated electrical energy efficiency (6.588 $kWhm^{-3}$ $order^{-1}$) of CeO_2/Fe_2O_3 CNS confirmed the consumption of less energy in degrading EY. Besides, the CeO_2-$/Fe_2O_3$ CNS exhibited a specific capacitance of 142.6 F g^{-1} at a scan rate of 5 mV s^{-1} and displayed excellent capacitance retention of 94.8% after 1000 cycles. Our results showed that the synthesized CeO_2/Fe_2O_3 CNS with enhanced visible light-driven photocatalytic activity and supercapacitive cycling stability could be a potential candidate for its use in environmental and energy storage applications.

Acknowledgements

This work was supported by the Technology Innovation Program (10041957, Design and Development of fibre-based flexible display) funded by the Ministry of Trade, industry & Energy (MI, Korea) and Civil-Military Technology Cooperation Center (13-DU-EE-13).

Notes and references

1 A. Fujishima and K. Honda, *Nature,* 1972, **238**, 37-38.
2 X. Xu, C. Randorn, P. Efstathiou and J. T. S. Irvine, *Nat. Mater.,* 2012, **238**, 595-598.
3 P. Furle, J. R. Scheffe and A. Steinfeld, *Energy Environ. Sci.,* 2012, 5, 6098-6103.
4 B. C. H. Steele, *Nature,* 1999, **400**, 619-621.
5 G. F. Li, Q. Y. Wang, B. Zhao, M. Q. Shen and R. X. Zhou, *J. Hazard. Mater.,* 2011, **186**, 911-920.
6 N. Izu, W. Shin, N. Murayama and S. Kanzaki, *Sensor. Actuat. B,* 2002, **87**, 95–98.
7 X. H. Lu, D. Z. Zheng, J. Y. Gan, Z. Q. Liu, C. L. Liang, P. Liu and Y. X. Tong, *J. Mater. Chem.,* 2010, **20**, 7118-7122.
8 A. Corma, P. Atienzar, H. Garcia and J. Y. C. Ching, *Nat. Mater.,* 2004, **3**, 394-397.
9 X. Lu, D. Zheng, P. Zhang, C. Liang, P. Liu and Y. Tong, *Chem. Commun.,* 2010, **46**, 7721–7723.
10 L. Mao, Y. Wang, Y. Zhong, J. Ning and Y. Hu, *J. Mater. Chem. A,* 2013, **1**, 8101-8104.
11 N.S. Arul, D. Mangalaraj and J. I. Han, *Mater. Lett.,* 2015, **145**, 189-192.
12 N. Zhang, S. Liu, X. Fu and Y. J. Xu, *J. Phys. Chem. C,* 2011, **115**, 22901-22909.
13 S. Ghasemi, S. R. Setayesh, A. H. Yangjeh, M. R. H. Nezhad and M. R. Gholami, *J. Hazard. Mater.,* 2012, **199-200**, 170-178.
14 C. Li, R. Chen, X. Zhang, S. Shu, J. Xiong, Y. Zheng and W. Dong, *Mater. Lett.,* 2011, **65**, 1327-1330.
15 N. Wetchakun, S. Chaiwichain, B. Inceesungyorn, K. Pingmuang, S. Phanichphant, A. I. Minett and J. Chen, *ACS Appl. Mater. Interfaces,* 2012, **4(7)**, 3718-3723.
16 Y. Jiao, Y. Liu, B. Yin, S. Zhang, F. Qu and X. Wu , *Nano Energy,* 2014, **10**, 90-98.
17 N. Padmanathan and S. Selladurai, *RSC Adv.,* 2014, **4**, 6527-6534.
18 L.S. Aravinda, K. U. Bhat and B. R. Bhat, *Mater. Lett.*, 2013, **112**, 158-161.
19 Y. Wang, C.X. Guo, J. Liu, T. Chen, H. Yang and C.M. Li, *Dalton Trans*., 2011, **40**, 6388-6391.
20 P. Luan, M. Xie, D. Liu, X. Fu and L. Jing, *Sci. Rep.,* 2014, **4**, 61801-7.
21 S. J. A. Moniz, S. A. Shevlin, X. An, Z. X. Guo and J. Tang, *Chem. Eur. J.,* 2014, **20**, 1-10.
22 H. Zhao, L. Zhang, X. Gu, S. Li, B. Li, H. Wang, J. Yang and J. Liu, *RSC Adv.,* 2015, **5**, 10951-10959.
23 S. Xie, F. Lu, N. Sun, S. Liu, H. Jia and L. Zheng, *CrystEngComm*., 2014., **16**, 9727-9734.
24 N. Nagarajan and I. Zhitomirsky, *J. Appl. Electrochem*., 2006, **36**, 1399-1405.
25 Z. Gu, K. Li, S. Qing, X. Zhu, Y. Wei, Y. Li and H. Wang, *RSC Adv.,* 2014, **4**, 47191–47199.
26 N. S. Arul, D. Mangalaraj, P. C. Chen, N. Ponpandian, P. Meena and Y. Masuda, *J. Sol-Gel Sci. Technol.,* 2012, **64**, 515-523.
27 J. Xin, C. Jia-Jia, X. Jian-Hui, S. Yi-Ning, F. You-Zuo and Z. Min-Sen, *Chem. Commun.,* 2012, **48**, 7410-7412.
28 O. M. Lemine, *Superlattice. Microst.,* 2009, **45**, 576-582.
29 N. S. Arul, D. Mangalaraj and T. W. Kim, *Appl. Phys. Lett.,* 2013, **102**, 223115-1- 223115-4.
30 G. Zhou, D. W. Wang, P. X. Hou, W. Li, N. Li, C. Liu, F. Li and H. M. Cheng, *J. Mater. Chem.,* 2012, **22**, 17942-17946.
31 J. Zhang, F. Huang and Z. Lin, *Nanoscale*, 2010, **2**, 18–34.
32 T.P. Almeida, M.W. Fay, Y. Zhu and P.D. Brown, *Nanoscale*, 2010, **2**, 2390–2399.
33 D. Zhang, F. Niu, T. Yan, L. Shi, X. Du, J. Fang, Appl. Surf. Sci., 2011, **257**, 10161-10167.
34 W. Yang, Y. Xu, Y. Tang, C. Wang, Y. Hu, L. Huang, J. Liu, J. Luo, H. Guo, Y. Chen, W. Shi and Y. Wang, *J. Mater. Chem. A*, 2014, **2**, 16030–16038.
35 S. Sun, X. Zhang, J. Zhang, L. Wang, X. Song and Z. Yang, CrystEngComm., 2013, 15, 867–877.
36 S. Tsunekawa, J.T. Wang and Y. Kawazoe, *J. Alloys Compd.,* 2006, **1145**, 408-412.
37 F. Meng, L. Wang and J. Cui, *J. Alloys Compd.,* 2013, **556**, 102-108.
38 A. P. Grosvenor, B. A. Kobe, M. C. Beisinger and N. S. Mclntyre, *Surf. Interface Anal.,* 2004, **36**, 1564-1574.
39 A. G. Nasibulin, S. Rackauskas, H. Jiang, Y. Tian, P. R. Mudimela, S. D. Shandakov, L. Nasibulina, J. Sainio and E. I. Kauppinen, *Nano Res.,* 2009, **2**, 373-379.
40 L. T. Murciano, A. Gilbank, B. Puertolas, T. Garcia, B. Solsona and D. Chadwick, *Appl. Catal., B Environ.,* 2013, **132–133**, 116-122.
41 A. Galtayries, R. Sporken, J. Riga, G. Blanchard and R. Caudano, *J. Electron. Spectrosc. Relat. Phenom.,* 1998, **88–91**, 951-956.
42 42 Z.M. Yang, G.F. Huang, W.Q. Huang, J.M. Wei, X.G. Yan, Y.Y. Liu, C. Jiao, Z. Wan and A. Pan, *J. Mater. Chem. A,* 2014, **2**, 1750–1756.
43 D. Channei, B. Inceesungvorn, N. Wetchakun, S. Ukritnukun, A. Nattestad, J. Chen and S. Phanichphant, *Sci. Rep.,* 2014, **4**, 5757-1-5757-7.
44 L. Zhu, M. Hong and G.W. Ho, *Nano Energy,* 2015, **11**, 28-37.
45 L. Li, J. Xu, C. Guo and Y. Zhang, *Front. Environ. Sci. Eng.,* 2013, **7**, 382-387.
46 S. Carter, M. I. Stefan, J. R. Bolton and A. S. Amiri, *Environ. Sci. Technol.,* 2000, **34**, 659-662.
47 Y. Xu and M. A. A. Schoonen, *Am. Mineral.,* 2000, **85**, 543-556.
48 J. W. Ko, J. H. Kim and C. B. Park, *J. Mater. Chem. A*, 2013,**1**, 241–245.
49 Q. Cheng, J. Tang, J. Ma, H. Zhang, N. Shinya and L.C. Qin, *Carbon,* 2011, **49**, 2917-2925.
50 J. Liu, J. Jiang, M. Bosman and H. J. Fan, *J. Mater. Chem.,* 2012, **22**, 2419-2426.
51 Y. Si and E.T. Samulski, *Chem. Mater.,* 2008, **20**, 6792-6797.
52 X. Zhang, X. Wang, L. Jiang, H. Wu, C. Wu and J. Su, *J. Power Sources,* 2012, **216**, 290-296.
53 J. Zhu and J. He, *ACS Appl. Mater. Interfaces,* 2012, **4**, 1770-1776.
54 K. Liang, N. Wang, M. Zhou, Z. Cao, T. Gu, Q. Zhang, X. Tang, W. Hu and B. Wei, *J. Mater. Chem. A,* 2013, **1**, 9730-9736.
55 P.A. Basnayaka, M.K. Ram, E.K. Stefanakos and A. Kumar, *Electrochim. Acta,* 2013, **92**, 376-382.
56 D. Han, P. Xu, X. Jing, J. Wang, D. Song, J. Liu and M. Zhang, *J. Solid. Chem.,* 2013, **203**, 60-67.
57 Q. Wang, L. Jiao, H. Du, Y. Si, Y. Wang and H. Yuan, *J. Mater. Chem.,* 2012, **22**, 21387-21391.
58 B. E. Conway, Electrochemical supercapacitor, Kluwer Academic/Plenum Publishers, New York, 1999.